Soft Matter

Temperature Effects on the Nanoindentation Characterization of Stiffness Gradients in Confined Polymers

Journal:	*Soft Matter*
Manuscript ID	SM-ART-07-2018-001539.R1
Article Type:	Paper
Date Submitted by the Author:	20-Oct-2018
Complete List of Authors:	Song, Jake; Northwestern University, Materials Science and Engineering; Massachusetts Institute of Technology, Materials Science and Technology Kahraman, Ridvan; Northwestern University, Materials Science and Engineering Collinson, David; Northwestern University, Mechanical Engineering; Duke University, Mechanical Engineering and Materials Science Xia, Wenjie; North Dakota State University, Civil and Environmental Engineering Brinson, L.; Duke University, Mechanical Engineering and Materials Science; National Institute of Standards and Technology, Center for Hierarchical Materials Design Keten, Sinan; Northwestern University, Mechanical Engineering; Northwestern University, Civil and Environmental Engineering; National Institute of Standards and Technology, Center for Hierarchical Materials Design

Temperature Effects on the Nanoindentation Characterization of Stiffness Gradients in Confined Polymers

Jake Song[ǂ¥&], Ridvan Kahraman[ǂ¥], David W. Collinson[£§¥], Wenjie Xia[€], L. Catherine Brinson[£$*] and Sinan Keten[§†$*]

[ǂ] Dept. of Materials Science & Engineering, Northwestern University, 2145 Sheridan Road, Evanston, IL 60208-3109

[†] Dept. of Civil & Environmental Engineering, Northwestern University, 2145 Sheridan Road, Evanston, IL 60208-3109

[$]Center for Hierarchical Materials Design, Northwestern University, 2145 Sheridan Road, Evanston, IL 60208-3109

[§] Dept. of Mechanical Engineering, Northwestern University, 2145 Sheridan Road, Evanston, IL 60208-3109

[£]Dept. of Mechanical Engineering and Materials Science, Duke University, 144 Hudson Hall, Durham, NC 27708

[€]Department of Civil & Environmental Engineering, North Dakota State University, Fargo, ND, 58108

[¥] These authors contributed equally to this work.

[&] Current Address: Dept. of Materials Science and Engineering, Massachusetts Institute of Technology, 77 Massachusetts Avenue, Cambridge, MA 02139

[*] Corresponding Author (current address): Dept. of Mechanical Engineering and Materials Science, Duke University, 144 Hudson Hall, Durham, NC 27708. Tel: 919-660-3933, E-mail: *cate.brinson@duke.edu*

[*] Corresponding Author: Dept. of Mechanical Engineering and Dept. of Civil & Environmental Engineering, Northwestern University, 2145 Sheridan Road, Evanston, IL 60208-3109. Tel: 847-491-5282, E-mail: *s-keten@northwestern.edu*

Abstract

The stiffening of polymers near inorganic fillers plays an important role in strengthening polymer nanocomposites, and recent advances in metrology have allowed us to sample such effects using local mechanical measurement techniques such as nanoindentation and atomic force microscopy. A general understanding of temperature and confinement effects on the measured stiffness gradient length-scale ξ_{int} is lacking however, which convolutes molecular interpretation of local property measurements. Using coarse-grained molecular dynamics and finite element nanoindentation simulations, we show that the measured ξ_{int} increases in highly confined polymer systems, a dependence which acts in the opposite direction in systems with low confinement. These disparate trends are closely related to the polymer's viscoelastic state and the resulting changes in incompressibility and dissipative ability as the polymer transitions from glassy to rubbery. At high temperatures near the glass transition temperature, a geometrically confined system restricts the activated volume in the polymer by the applied load in the increasingly incompressible polymer. This causes a dramatic build-up of hydrostatic pressure near the confining surface, which contributes to an enlarged measurement of ξ_{int}. By contrast, a less-confined system allows the pressure to dissipate via intermolecular motion, thus lowering the measured ξ_{int} with increased temperature above the glass transition temperature. These findings suggest that the well-established thin-film nanocomposite analogy for polymer mobility near interfaces can be convoluted when measuring local mechanical properties, as the viscoelastic state and geometric confinement of the polymer can impact the nanomechanical response during indentation.

1. Introduction

The interfacial stiffening of polymer molecules near rigid surfaces is of great interest for a wide range of soft materials including polymer thin films[1, 2] and nanocomposites.[3] Recent advances in experimental and simulation techniques have enabled the local measurement of stiffness gradients in polymer-particle interphases.[4-12] However, the reported extents of the stiffened length-scale, ξ_{int}, differ considerably, based on atomic force microscopy, fluorescence and simulations methods. A selection of these studies are summarized in Table 1. These studies operate in different conditions such as sample size, substrate type, indentation depth, and employ different indenter tip sizes and geometries which can affect the measured ξ_{int} via stress field interactions.[10] Importantly, they also generally sample different viscoelastic states of polymers. For example, a range of polymers (poly(methyl methacrylate) (PMMA),[6, 10] polystyrene (PS),[7] poly(ethyl methacrylate) (PEMA) and poly(isobutyl methacrylate) (PiBMA) mixtures,[11] poly(vinyl acetate) (PVAc),[13] and styrene-butadiene rubber (SBR)[12]) have been sampled at a large range of indentation rates (5Hz to 125,000 kHz) and at different temperatures relative to their glass transition temperature T_g, thus constituting various states of polymer viscoelasticity. Moreover, some systems are characterized in a supported thin film state[4-6, 10, 12, 14] while others are characterized directly in a nanocomposite state.[11, 15]

Table 1. Summary of previous studies on the length scale of the measured interphase in confined polymers via local measurements. Each study attempts different methods to account for structural effects, which are not detailed here.

Polymer	Filler	Surface Treatment	Stiffness Gradient Length (nm)	Technique	Sampling Rate (Hz)	Viscoelastic State[a]	Geometry[b]
PMMA	Alumina	-	100[6]	AFM	2k	Glassy	TkFW
PMMA	Silica	-	170[6]	AFM	2k	Glassy	TkFW
PS	Glass	-	80[7]	AFM	2k	Glassy	TkFW
PS	Glass	-	45-85/85-200[8,c]	Fluorescence	-	Glassy to Rubbery	TnF (20-935nm)
PMMA	Fixed Wall	~170mJ/m^2	33-62[9]	MD	5ms^{-1}	Glassy	TnFW (40nm)
PEMA/ PiBMA	40nm Silica	DMDCS	30-35 to 55-70[10,d]	AFM	20, 333	Glassy to Rubbery	PNC
SBR	Silicon	Silane/ thiol-ene	40[11]	AFM/FEA	~100	Rubbery	TkFW
PVAc	Silicon	-	18/~100[12,e]	AFM	5.5	Rubbery	TnF (9-610nm)
PVAc	12.5nm SiO_2	-	~2-3[15]	AFM	277-367k	Glassy	PNC

Notes: [a]Transition region is defined to be within 20°C of T_g.[b]TkFW=Thick film w/ neighboring wall, PNC = polymer nanocomposite, TnFW = thin film with neighboring wall, TnF = supported thin film. [c]45-85nm measured in the glassy and transition states; 85-200nm measured in the rubbery state.[d]30-35nm measured at 25°C below the T_g; 55-70nm measured at 22°C above the T_g.[e]18nm measured with a tip radius of 12nm;~100nm measured with a tip radius of 150nm.

While seminal studies have confirmed a thin film-nanocomposite analogy in the context of T_g gradients,[16] it is unclear if the same relationship can be gleaned from local nanomechanical analyses. Global mechanical analyses on thin films via methods such as thin film wrinkling[2, 17] and simulations have shown that the interphase length is on the order of a few tens of nanometers at most, contradicting the relatively large stiffness gradient length-scales predicted by more local measurements such as indentation (Table 1). While local measurements ideally report only the local inherent change in the polymer stiffness due to chemical and molecular confinement effects, the impact of stress field interactions of the probed volume with the substrate, the indenter tip itself, or the rigid supporting surface can be reflected in the measured stiffness values and thus ξ_{int}. Some recent work has begun to decouple these effects by incorporating simple simulations with experimental data.[12, 14] However, due to the critical lack of understanding of the effect of the

polymer's viscoelastic state and geometric confinement on such stress field interactions, it remains challenging to extract this molecular component of the mechanical interphase in polymer nanocomposites. We aim to explicitly demonstrate these complexities to the measured ξ_{int} here and evaluate the combined effect of polymer thermal states (relative to their T_g) and degree of confinement from nearby surfaces on local stiffness measurements.

2. Method

2.1 Model Considerations

The configuration considered here is a "model nanocomposite" often used in experimental studies. Such a system consists of a polymer film supported on a substrate of interest which acts as a particle mimic. A flat surface is prepared across the substrate – polymer interface, and an AFM tip then rasters across the substrate and the neighboring polymer to report the stiffness gradient in the polymer and its length scale ξ_{int}. This work undertakes numerical simulations of AFM indentation on model nanocomposite samples to address the challenges mentioned in the introduction.

2.2 Molecular Dynamics Setup

To capture the experimental model nanocomposite in molecular dynamics (MD) simulations, we create polymer films in contact with an energetic rigid substrate on the xy plane of the film supported by a rigid wall at the bottom, with film thickness of 20nm to enable tractable computation times (Fig. 1A). The coarse-grained (CG) PMMA[18] molecules have a molecular mass of ~10 kDa (Fig. 1A inset). Relevant force-field data for the CG model can be found in the Supporting Information. The interfacial polymers are confined from moving in the x and y directions by hard springs with a very high spring constant of 1000 kcal/mol-Å^2 to prevent

polymers creeping over the energetic substrate, and to provide structural support on the bottom during indentation. The spring constant on the bottom rigid wall is lowered to 0.5 kcal/mol-Å^2 to mimic weaker confinement scenarios. The polymers near the energetic substrate are allowed to move freely in the z direction and interact with the substrate with a 12-6 Lennard Jones (LJ) potential of the form

$$U_{sub}(z) = 4\varepsilon_{sp}\left[\left(\frac{\sigma_{sub}}{z}\right)^{12} - \left(\frac{\sigma_{sub}}{z}\right)^{6}\right] \qquad z < z_{cut} \tag{2}$$

where z is the distance of the atoms from the substrate, $\sigma_{sub} = 4.5$ Å is the distance where U_{sub} is zero, and ε_{sp} is the strength of the interfacial interaction between substrate and polymer. Similar to our prior work, ε_{sp} is set to be 5 kcal/mol – corresponding to a surface energy of ~ 170 mJ/m^2 which can be obtained experimentally via surface functionalization.[10] The film is relaxed by minimization via the conjugate gradient algorithm, followed by an annealing cycle between 250 K and 400 K under the NVT ensemble and an equilibration process at 300 K for 2 ns.

To sample various thermal state points of the polymer, we vary the temperature T of the film from 150 K to 450 K, a range which spans below and above the CG polymer's T_g of ≈ 385 K[18]. MD methods can only access a limited range of time scales even with CG methods, but since time and temperature are interrelated in describing polymer dynamics,[19] ramping the temperature of the system provides a facile way to access the rubbery response of polymers. After equilibration, cylindrical indenters of radius R = 20 nm that extend along the y-axis are placed roughly 2 nm above the film, and then loaded onto the film at a velocity of $v = 5$ m/s (corresponding to a strain rate of about 2.5×10^8 s^{-1}) with depth $d < 5$ nm at varying distance z from the substrate (Fig. 1A). The cylindrical indenters are constructed via the carbon nanotube generator in the VMD software to mimic experimental carbon-based indenters (e.g. a diamond indenter).[20] The carbon

indenters are assumed to be rigid, and interact weakly with the polymer with the same LJ potential form as Eqn. 1., but with distance r and tip-polymer interaction strength ε_i in place of z and ε_{sp} respectively. The indenters interact weakly with the polymer with an interaction strength $\varepsilon_i = 0.1$ kcal/mol to mimic weak interactions corresponding to a surface energy of ~ 27 mJ/m^2 between indenter and polymer. We find that varying ε_i has only a minor effect on the stress response and the resulting ξ_{int} (Fig. S1). After indentation, force-displacement (F-d) data from the loading curve are fitted with a linear function at $d < 3$ nm to obtain the stiffness k, i.e. the slope. This approach has been recently utilized to obtain mechanical property gradients.[12] In similar vein to our prior work,[10] we normalize the local stiffness measurements by the bulk value k_0 (where $k(z)$ converges to a plateau) to determine ξ_{int} using the following function:

$$\frac{k}{k_0} = 1 + A\exp\left(-\frac{z}{\zeta}\right) \tag{3}$$

where A is a fitting constant that controls the magnitude of the stiffness at the interface, and ζ is a fitting constant that controls the rate of decay as a function of distance from the substrate, z. ξ_{int} is defined as the distance where $\frac{k}{k_0} = 1.01$.

2.3 Finite Element Analysis Model

The finite element analysis (FEA) model was built to closely resemble the molecular dynamics (MD) model, but also including variability of sample size to reflect typical experimental conditions. FEA is a widely used simulation tool for modeling tip indentation in polymer films and composites, with previous studies[4, 9, 21-23] utilizing FEA software to better understand the continuum level response of a system to indentation. The system was solved using ABAQUS™ software (Fig. 1C). The system was modelled in Cartesian 2D space with a general plane strain assumption. The initial film model was specified to be 600 nm thick and 600 nm wide, which while

not as large as many experimental samples, is large enough to avoid boundary effects from the bottom and the far edge. To mimic the thin film used in MD, a model was created where the film thickness and width was reduced to 20 nm and 200 nm respectively. Both systems used a fixed boundary condition to model a stiff substrate. The model was chosen to minimize computation time while ensuring that the boundary conditions applied to the model edges did not undesirably affect the structural compliance of the system. The tip was modelled as an elastic semi-circle with a 20 nm radius. The base of the model was fully fixed as a boundary condition. The left-hand edge of the substrate was constrained in the horizontal direction. It was assumed that the PMMA and the substrate were perfectly bonded, so no separation occurred. Each indentation was conducted by a linear ramp over 0.1 s to the nodes of the tip until a maximum displacement of 5 nm was achieved. It is estimated that this ramp rate was approximately equivalent to a triangular wave frequency of 2.5 Hz. The rate of indentation used in the FEA is therefore significantly lower than the indentation rate used in the MD ($50 nms^{-1}$ and $5 ms^{-1}$ respectively). The MD-CG model is parameterized such that non-glassy viscoelastic behavior is observable at such high strain rates.

The contact between the tip and the polymer was modelled with a soft contact model called exponential pressure-overclosure relation ($c_0 = 0.001, p_0 = 5e9$). The slip behavior was modelled with the penalty method and a specified friction coefficient of 0.25 was used to represent the low adhesion expected between the tip and the glassy PMMA.

An elastic-viscoelastic material model was applied to the polymer region to model the PMMA response. The instantaneous response was specified with a Young's modulus ($E_0 = 2.31\,\text{GPa}$) and a Poisson's ratio ($\upsilon = 0.35$). The substrate and the AFM tip were simulated as purely elastic glass ($E_{sub} = 73\,\text{GPa},\ \upsilon_{sub} = 0.3$) and silicon ($E_{tip} = 150\,\text{GPa},\ \upsilon_{tip} = 0.3$)

respectively. The viscoelastic response was modelled by fitting a 40-term Prony series to experimental data (Fig. 1C) obtained with dynamic mechanical analysis (TA Instruments, USA) using the NanoMine[24, 25] tool 'dynamfit'. To obtain the experimental viscoelastic properties of PMMA, a sample of PMMA was mounted into the DMA and a pre-strain of 0.02 % was applied. The sample temperature was then ramped from 298 K to 443 K in 5 K intervals and a frequency sweep from 0.01 Hz to 80 Hz was conducted. Time-temperature superposition was used to produce a master curve and the corresponding shift factors from the collected data. Stiffness values were obtained using the same protocol with the MD simulations and normalized with the bulk stiffness value in the far-field.

The mesh elements used for the system were CPE4R elements. The mesh was refined near the indentation location to improve the accuracy of the result. An explicit solver was chosen to find a solution for the system as an explicit solver was found to be more efficient than the implicit solver in ABAQUS for this system. Due to the slow indentation speed, the kinetic energy in the system was less than 5% of the internal energy; therefore, this regime successfully approximates the quasi-static solution. The kinetic energy was also observed to be significantly lower than the total system energy, suggesting that the dynamic contributions are insignificant.

To draw a qualitative comparison between FEA and MD simulations, tan δ values of the FEA and MD systems were matched at four temperatures (Fig. S3) by performing time-temperature superposition on the master curve obtained from the DMA (Fig. 1B). By shifting the master curve to an appropriate temperature, it is possible to adjust the loss tangent of the material model used in the FEA to match the loss tangent measured with CG-MD while maintaining a single indentation rate. The values for the FEA temperatures are 392 K, 395.6 K, 401.1 K and 407 K, which match the MD tan δ values at temperatures of 300 K, 350 K, 400 K and 450 K

respectively (see Section 2.4 for protocol). Linear interpolation between shift factors was used to shift the master curve to the temperatures suitable for comparison with MD.

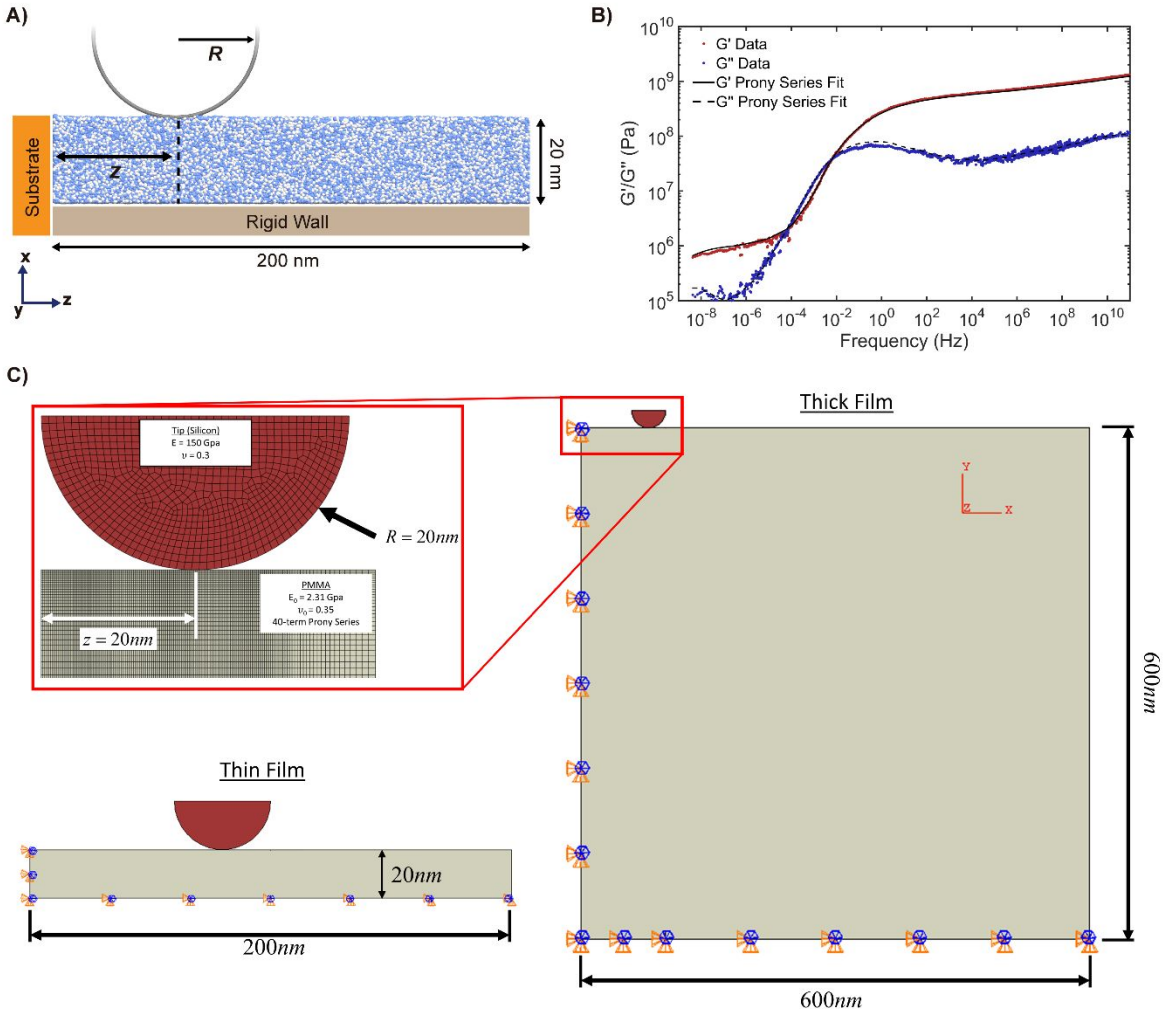

Figure 1. Simulation setup for nanoindentation study of the confined polymer. (A) Simulation setup for the indentation study in MD. A carbon-based indenter of radius R is used to indent the polymer at varying distances away from the substrate (z) to probe the interphase length-scale ξ_{int}. (B). Experimental frequency-dependent data determined via bulk DMA for a PMMA sample shifted with time-temperature superposition to a reference temperature of 393 K and the corresponding fit produced by a 40-term Prony Series. (C) FEA indentation model. The AFM tip

region is red and the PMMA region is off-white. The boundary is indicated by the cones along the edge of the model where required. The $z = 20\ nm$ location is used to analyze the stress field as it is the closest point to the substrate studied where the tip does not directly interact with the side boundary condition. The mesh is suppressed in the thick and thin film schematics for clarity.

2.4 Details and Analysis of Molecular Dynamics Simulation

To probe the viscoelastic response of poly(methyl methacrylate) (PMMA) at the same conditions as those used for indentation simulations, small amplitude oscillatory shear (SAOS) simulations are performed on bulk coarse-grained (CG) PMMA in the NVT ensemble using the SLLOD algorithm.[20, 26] 5,000 CG-PMMA monomers with periodic boundary conditions in all axes are relaxed by the process described in Section 2.2. Subsequently, 40 sinusoidal oscillations are performed at the same frequency as the indentation strain rate (i.e. $f = 2.5 \times 10^8\ \mathrm{s}^{-1}$) at a small amplitude of $\gamma_0 =$ 0.03. The amplitude value is within the range of the linear viscoelastic regime predicted by both prior work and our recent study for CG polymers.[27, 28] The shear stress outputs are fitted with a sinusoidal function $\sigma_{xy} = \sigma_0 \sin(2\pi f t + \delta)$ using the least-square method to obtain the loss tangent δ, the storage modulus $G' = \sigma_0 \cos(\delta)/\gamma_0$, and the loss modulus $G'' = \sigma_0 \sin(\delta)/\gamma_0$ at variable temperatures. Further discussions on the choice of γ_0 and fitting procedures for finding G' and G'' in this manner is discussed at length in our recent work.[27]

The incompressibility of our MD model can be analysed by calculating the isothermal bulk modulus $B = -V\left(\frac{dP}{dV}\right)_T$, and the Poisson's ratio ν. To calculate B, we use the methods of Allen and Tildesley:[29]

$$B = k_B T \frac{< V >}{< \delta V >^2} \quad (4)$$

where k_B is the Boltzmann constant, and $< V >$ and $< \delta V >$ are the ensemble-averaged volume and the standard deviation of volume, respectively. We track $< V >$ and $< \delta V >$ of a relaxed system in the *NPT* ensemble at every time step (4 fs) for 1 ns. Upon obtaining *B*, ν can be calculated by the following relation:

$$\nu = \frac{3B - 2G^*(f)}{6B + 2G^*(f)} \quad (5)$$

Where $G^*(f)$ is the complex shear modulus obtained from our SAOS simulations at $f = 2.5 \times 10^8$ Hz which is consistent with the strain rate of indentation. A rate-dependent complex shear modulus is used in the above relation instead of the (instantaneous) shear modulus *G* as it better reflects the deformation conditions of the MD model during indentation.

The stress values are obtained from atomic virial stress tensors:

$$\sigma_{ij} = -\frac{1}{V}\left[\sum_{A}^{n} m_A (v_A)_i (v_A)_j + \sum_{A>B}^{n} \frac{\partial U}{\partial r_{AB}} \frac{(r_{AB})_i (r_{AB})_j}{r_{AB}}\right] \quad (6)$$

where *V* is the volume of the film, *n* is the total number of CG beads, r_{AB} is the distance between bead pair *A* and *B*, *U* is the total energy of the system, and m_A and v_A denote the mass and velocity of *A*th bead, respectively. The Von Mises stress is calculated by the following:

$$\sigma_v = \sqrt{\frac{\left(\sigma_x - \sigma_y\right)^2 + \left(\sigma_y - \sigma_z\right)^2 + \left(\sigma_z - \sigma_x\right)^2 + 6\left(\sigma_{xy}{}^2 + \sigma_{yz}{}^2 + \sigma_{xz}{}^2\right)}{2}} \quad (7)$$

The local strains are computed using the method proposed by Falk and Langer, using the open molecular visualization tool OVITO.[30-32] A local strain value for each CG atom *i* is obtained

by summing over its neighboring atoms within a set radius of 2.5 σ and computing the relative displacements of these particles relative to *i* during the $d < 4\ nm$ indentation simulation. A strain tensor is then calculated by minimizing the difference of real displacements and affine displacements that would result from this strain tensor. Equivalent Von Mises strains are plotted using the Von Mises equation

$$\varepsilon_{eq} = \frac{1}{\sqrt{2}(1+\upsilon')}\sqrt{(\varepsilon_x - \varepsilon_y)^2 + (\varepsilon_y - \varepsilon_z)^2 + (\varepsilon_z - \varepsilon_x)^2 + \frac{3}{2}(\gamma_{xy}^2 + \gamma_{yz}^2 + \gamma_{xz}^2)} \quad (8)$$

where the shear components γ_{ij} are equal to $2\varepsilon_{ij}$, and υ' is the Poisson's ratio.

The hydrostatic pressure stress is calculated for each element in the FEA as follows:

$$p = -\frac{1}{3}trace(\overline{\overline{\sigma}}) \quad (9)$$

Where $\overline{\overline{\sigma}}$ is the stress tensor obtained from the virial, and p is the equivalent pressure stress.

For MD hydrostatic pressure fields, the hydrostatic pressure contribution of each CG bead is calculated using:

$$p_{bead} = -\frac{1}{3}trace(\overline{\overline{\sigma}}_{bead}) \quad (10)$$

Where $\overline{\overline{\sigma}}_{bead}$ is the Cauchy stress tensor, and is the equivalent pressure stress for each CG bead. The film is divided into regions of 2.5x2.5 nm length in the *x* and *y* directions and 10 nm in the *z* direction, and the average hydrostatic pressure in each region is then calculated.

3. Results and Discussion

We first performed an indentation sweep on the MD model to understand the viscoelastic state dependence of a highly-confined model nanocomposite. The normalized local stiffness profiles of the polymer with increasing temperature T (Fig. 2) show both a larger stiffness magnitude near the substrate and a broader decay function corresponding to larger ξ_{int}. The ξ_{int} values reported by the MD simulations in this manner report the overall stiffening of the polymer near the interface. We note here that using a different tip size or different ξ_{int} cut-off definition than what we used – R = 20 nm and 1% of the bulk value respectively – would affect the quantitative measurement of ξ_{int}. However, these features are systematic to the measurement,[10] and stand independent to the bulk (thermal) properties of the polymer film which are of interest to the study.

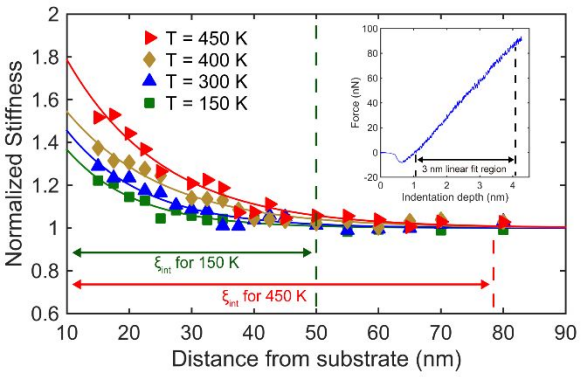

Figure 2. Normalized stiffness measurements obtained from indenting the PMMA at different distances away from the substrate at various temperatures. ξ_{int} values obtained from Eqn. 1 are 50 nm, 58 nm, 74 nm, and 78 nm for T = 150 K, 300 K, 400 K and 450 K, respectively. Only four temperatures are shown for clarity in presentation. (Inset) A force-displacement curve obtained from loading the polymer (R = 20 nm and z = 50 nm) using a tip-polymer interaction strength ε_i = 0.1 kcal/mol. Stiffness is obtained from fitting the linear region as denoted in the figure.

The ξ_{int} values show a non-linear increase with T, increasing slowly at low T, rapidly at intermediate T, and plateauing at higher T (Fig. 3A). To understand the correlation between the viscoelastic state of the polymer and ξ_{int}, we probe the dynamic properties of the CG polymer at

bulk state using small-amplitude oscillatory shear (SAOS). Equivalence with the indentation situation is not assumed *a priori,* as viscoelastic properties are obtained from shear studies on bulk PMMA (Section 2.4) would not be identical to those pertinent during indentation of confined PMMA due to different velocity fields and boundary conditions. Nevertheless, the agreement seems good: the decline in storage modulus $G'$and increase in loss modulus G'' with increasing temperature – signaling the onset of a rubbery transition in the polymer – occur between $T = 350$ K and 375 K, roughly where the ξ_{int} begins to spike (Fig. 3A). The good correlation observed here implies that the effect of temperature on ξ_{int} is fundamentally embedded in the polymer's viscoelastic state, wherein an increase in T above T_g will cause an increase in measured ξ_{int}. These results are consistent with recent studies that used PEMA-PiBMA polymers, in which this behaviour was correlated with the onset of glass transition in the polymer.[11] Another measure of T-dependent polymer dynamics that we can probe is the caging stiffness of the polymers; this is captured by the vibrational force constant f of the polymer which is related to the picosecond mean-squared displacement $\langle u^2 \rangle$ of the polymer (Fig. S2A). As discussed in the SI, there is a negative correlation between f and ξ_{int} of the polymer in the glassy regime – consistent with the findings of Chung et al.,[33, 34] – but nonlinearity ensues above the T_g (Fig. S2B).

While our results thus far are consistent with those of Huang et al.[11], there is currently no satisfactory explanation as to why a material at higher T with concomitantly larger viscoelastic dissipation due to greater intermolecular motion should exhibit a larger observed ξ_{int}. In fact, since stress can be more readily dissipated, one would expect lower ξ_{int} values. To understand other underlying factors behind our results, we also analyzed the bulk modulus B as a function of T via MD. Our calculations show that B is almost invariant with T, in agreement with the well-established continuum scale relationship of bulk modulus with temperature[35] whereas the complex

shear modulus $G^* = G' + iG''$ drops rapidly after the aforementioned transition point near T = 350 K ~ 375 K (Fig. 3B). The contrast in behaviour between the bulk modulus and shear modulus with temperature is thought to be due to the bulk modulus arising from intramolecular relaxations whereas the shear modulus is the result of intermolecular relaxations[35]. As such, the material's incompressibility increases, manifested by the increasing Poisson's ratio ν (Equation 4) with T. These trends are in excellent agreement with prior experimental findings on PMMA.[36] We note that the magnitude of ν is noticeably higher than the experimental counterpart below T_g: $\nu = 0.42$ at T = 300 K via MD compared to the commonly accepted literature value of $\nu = 0.35$. This suggests that B derived from our CG model is higher than experimental values, which is not surprising as the CG model used here is not explicitly parameterized to capture thermomechanical properties such as isothermal compressibility. We expect that employing a temperature-tuned CG model would result in achieving better agreement with the experimental values. With B plotted alongside ξ_{int}, we observe that there is an almost identical scaling of ν and ξ_{int} with T (Fig. 3C). This result supports the idea that an increase in incompressibility causes a non-localized deformation of polymers upon indentation, which promotes the transfer of load through the material and to the confining substrate on the left and results in an increased measurement of stiffness. As ν reaches a plateau with high T, so does the ξ_{int}, which also corroborates the correlation. These findings are consistent with numerical predictions of Clifford et al., who have also demonstrated that substrates are sensed sooner for high ν compliant layers supported on rigid substrates than low ν compliant layers.[37]

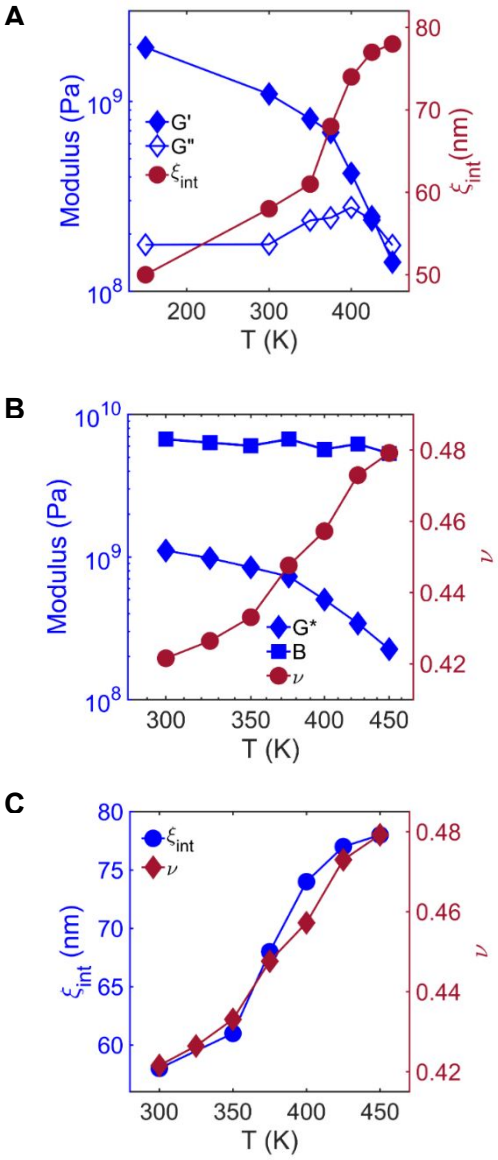

Figure 3. Observation of direct correlation between thermally-induced incompressibility of the confined polymer and the observed stiffness gradient length-scale ξ_{int}. (A) ξ_{int} values plotted alongside G' and G'" measured via small amplitude oscillator shear tests. The sudden increase in ξ_{int} at T = 350 K is marked by a sharp decline in G' and increase in G" at similar temperatures. (B) Bulk modulus B and complex shear modulus G^* of the polymer plotted alongside the resulting Poisson's ratio ν. (C) ξ_{int} values plotted alongside ν.

To confirm the onset of non-localized deformations at higher T we analyse Von Mises stress and strain fields upon indenting the polymer. As T is increased from 300 K to 450 K, we see that the activated Von Mises stress field under the indenter gradually becomes less noticeable (Fig. 4A) which is indicative of decreasing ability of the polymer to store the stress in a localized volume. This dissipation of the stress field is consistent with the decrease in storage modulus and increase in loss modulus with T (Fig. 3A). Simultaneously, we observe an increase in the range and

magnitude of local strain (Fig. 4B), in agreement with the increased incompressibility with the polymer (Fig. 3B).

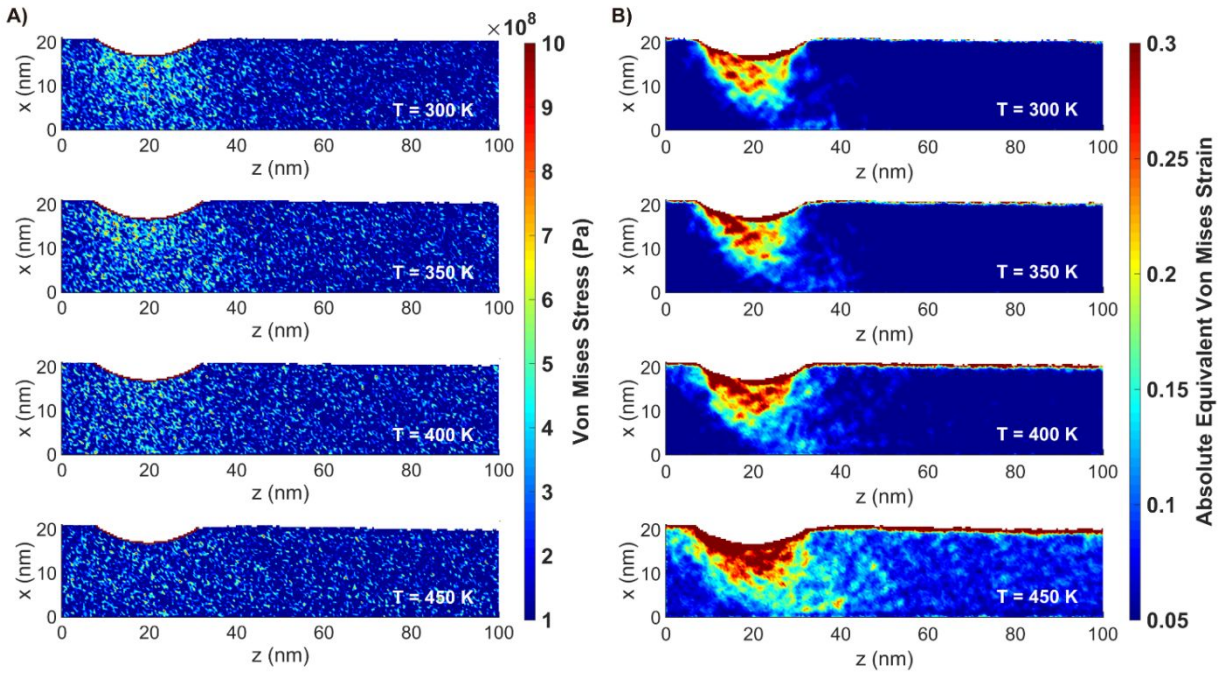

Figure 4. Von Mises stress and strain field plots during nanoindentation simulations at varying simulation temperatures. (A) Von Mises stress field obtained from atomic virial stress tensors during indentation, and (B) Von Mises strain field obtained from local strain tensors via the Falk and Langer method (see SI for calculation procedures). Note that the strain values are absolute. Both plots are generated at $d \sim 4$ nm using a $R = 20$ nm indenter at z = 20 nm.

Interestingly, these observations imply contradictory conclusions on the T-dependent trend of ξ_{int}: the viscous dissipation of stress should result in a lower ξ_{int} while the incompressibility of the highly confined polymer should lead to a higher ξ_{int} at higher T[21] due to the increased influence of B on the polymer response to indentation. The current MD results (Fig. 3C) alone clearly indicate that incompressibility dominates in competition with dissipation. We hypothesize that there is a mechanism that is dictating the outcome of this competition in favor of incompressibility, namely the degree of confinement in these very thin (20nm) systems. One method to test this

hypothesis is to increase the film thickness of the system; should our hypothesis be true; the trend should reverse and ξ_{int} should decrease at higher T for very thick films as there is more volume for the film to dissipate stress without the activated volume confined due to a substrate on the side or bottom of the film. Such a study can be done via FEA simulations, which is suitable for our study as the strong correlations between trends in bulk properties and locally measured mechanical properties in our current results strongly suggest a continuum level effect.

Next, we use FEA simulations to corroborate our MD simulation results, thereby accessing larger length-scales to analyze the effect of the confining surface on the bottom by varying the film thickness (the same analysis is not possible via MD due to computational limitations, as will be discussed later). However, a direct comparison between MD and FEA is challenging since, without explicit calibration of temperature and time effects, a CG-MD model will experience accelerated dynamics compared to an experimental polymer system due to its reduced degrees of freedom[27]. The trends in stress and strain fields from FEA indentation simulations using experimental indentation rates of 2.5 Hz at $\tan\delta$-equivalent temperatures (Fig. S3B and S3C) agree with CG-MD results (Fig. 4). We also find that the stress and strain fields from FEA simulations using an elastic PMMA model instead of the Prony series model shows a similar trend with a decreasing stress field and increasing strain field with T (Fig. S4). We note that these FEA simulations do not account for interaction between the substrate and polymer as the MD simulations do, and the input polymer modulus for the film is spatially uniform; thus, the change in the local stress and strain fields are due solely the changing bulk properties of the polymer with temperature and the effect of a close confining surface with incompressibility.

To partition the effects of viscous dissipation and incompressibility, we perform FEA indentation simulations on two systems: 20 nm and 600 nm thick films. The 600 nm thick film

represents the case where there is little to no confinement at the bottom, in contrast to the 20 nm film case that is currently studied in CG-MD (Fig. 1A and 1C). First, we analyze the hydrostatic pressure fields (i.e. first Cauchy stress invariant) of these simulations where the distance of the indenter is 20 nm from the substrate (Fig. 5A). The hydrostatic pressure fields are a direct visualization of the resistance to volume change (i.e. incompressibility) of the material, which helps us in understanding the change in broadening behavior of the measured stiffness length-scale between the thick and thin films. There is a dramatic increase in the build-up of hydrostatic pressure in the high-confinement case (Fig. 5A) which is noticeably prominent at the bottom and at the bottom-left corner of the polymer system, compared to the low-confinement case (Fig. 5B) where the pressure is allowed to dissipate throughout the film. In an analogous fashion, we perform hydrostatic pressure field calculations from MD simulations (Fig. 5C) with the protocols discussed in the SI. The MD analysis is noisier due to local fluctuations of the molecular chains, however mean-field averaging of the pressure fields in larger grid blocks also reveal an increase in the pressure in the bottom-left corner region at high T, in agreement with FEA results. To complement this finding, we study the change in local density in the MD model under the indenter upon indentation at various T (Fig. 5D). The film is divided by vertical dividers into rectangular regions of 2.5nm thickness, and the average density of CG polymer beads in each region is plotted as a function of distance from the substrate after being normalized to the average bulk density of the film at the same T. At low T, a significant increase in density underneath the indented area upon indentation is observed, indicating the compression of the polymer film. The extent of this compression-induced density decreases with T, which is in good correlation with the increased incompressibility of the polymer at these thermal states (Fig. 3B).

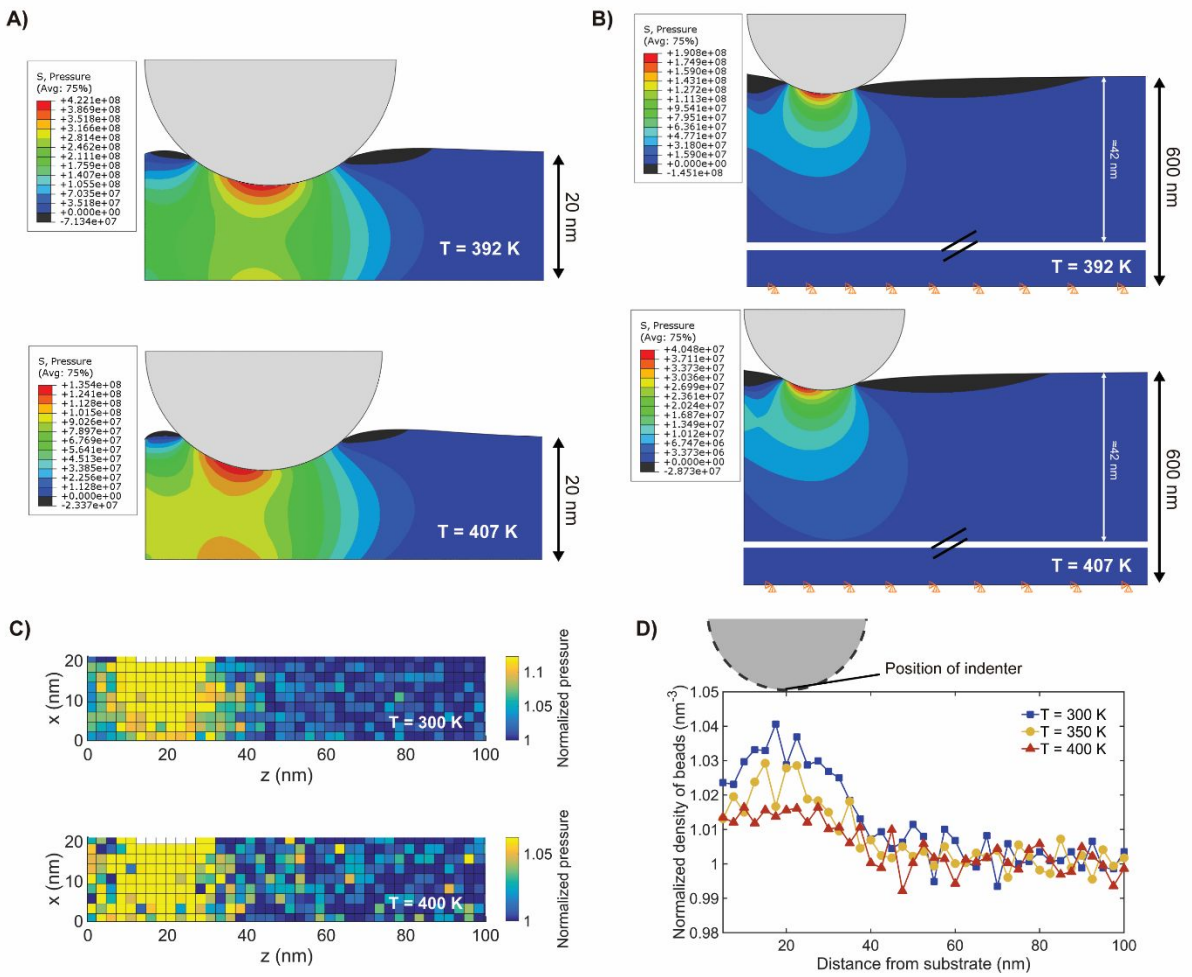

Figure 5. Observation of hydrostatic pressure build-up in high-confinement systems, in contrast to low-confinement systems where pressure dissipates through the material. FEA hydrostatic pressure fields for (A) the 20 nm thick and (B) the 600 nm thick PMMA films. (C) MD Hydrostatic pressure fields for the 20 nm thick film, normalized to the average bulk pressure before indentation. (D) Density of CG beads in the film upon MD indentation at different temperatures. Each point is normalized to the average density of the non-indented film at that temperature. All plots are generated at $d \sim 4$ nm using a $R = 20$ nm indenter at z = 20 nm.

Finally, we performed indentation sweeps across the substrate in FEA to relate the impact of T and incompressibility with ξ_{int} for differing levels of confinement. Since the input polymer properties are uniform for the FEA and no chemical interaction with the substrate can be considered, the increased measured apparent stiffness values and the ξ_{int} from the FEA simulation

is due entirely to stress field interaction effects of the probed volume with the lateral substrate and, in the case of 20nm thin film, the rigid supporting surface. As discussed previously, high-confinement and low-confinement systems are simulated in FEA by using a thin and thick film, respectively (Fig. 6A). In these simulations we also investigated the influence of dissipation on the substrate effect by comparing indentation sweeps using the PMMA model that included a Prony series describing the viscoelastic response, and a purely elastic PMMA model lacking viscous dissipation due to the time-dependent terms in the Prony Series (Fig. 6C). Overall, we find that the high-confinement FEA results (Fig. 6B) are in excellent agreement with the high-confinement MD results (Fig. 6D and 2) in showing a pronounced increase in ξ_{int} with T. Strikingly, we notice the opposite trend, and ξ_{int} decreases in the absence of strong confinement with T, as hypothesized earlier (Fig. 6C) when viscoelastic effects are included (via Prony series). In the purely elastic indentation sweeps across a thick film without viscous dissipation included in the material model, we see instead see the opposite trend and a slight increase in the substrate effect with increasing T. These results confirm that there are competing effects determining the magnitude of the substrate effect in polymer systems, incompressibility and dissipation, and that degree of confinement differentiates their relative impacts. The impact of polymer softening at high temperatures on ξ_{int} was also investigated and found to be insignificant within the range of temperatures examined.

At low T, polymers deform and compress locally and the measured stiffness gradient is strongly influenced by the stress field.[10] At high T, an onset of incompressibility reduces the ability of the polymer to compress locally, and increases the load required to indent the polymer. In a low confinement system, the viscoelastic polymer is able to dissipate load throughout the material volume. Therefore, incompressibility does not play a dominating role, and as T and dissipation

increase, the substrate effect decreases (Fig. 6C). In contrast, the polymer cannot dissipate stress freely in a high-confinement system due to geometric obstacles, causing the polymer to push against the confining surface on the bottom and driving up the hydrostatic pressure (Fig. 5A and 5C). This exacerbates the interaction with the energetic lateral substrate, as shown by the pressure build-up in the corners of systems in Fig. 5A and 5C, and enhances the local stiffness response. Thus, the suppression of dissipative effects in high-confinement systems cause an increase in ξ_{int} with T (Fig. 6B and 6D).

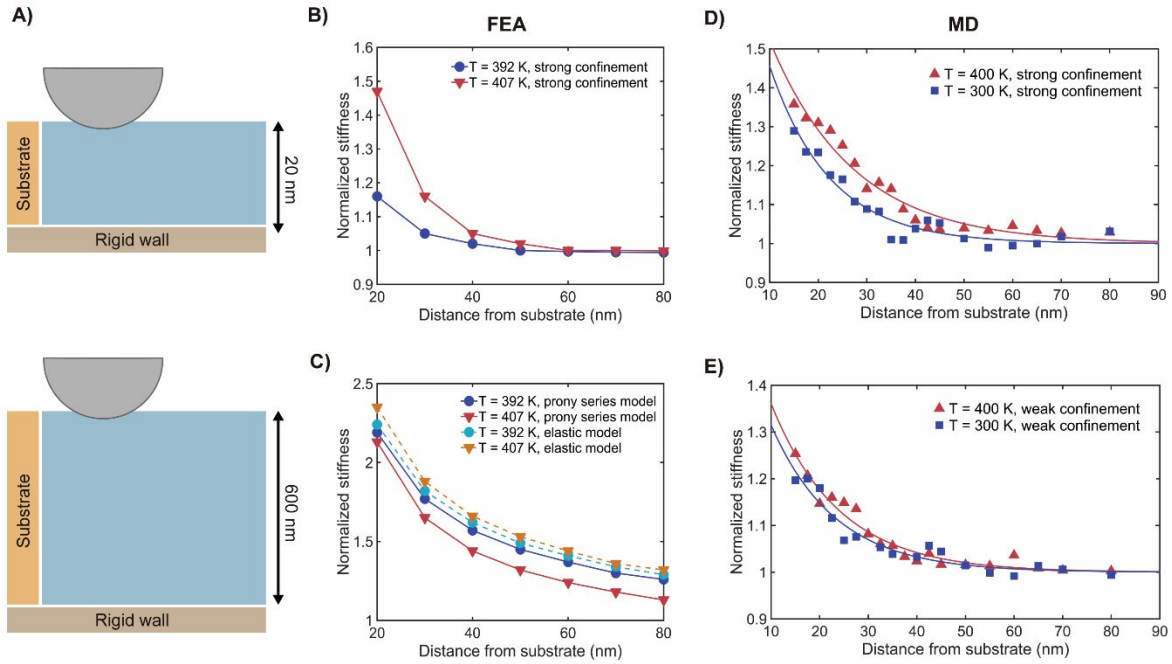

Figure 6. Divergence in *T*-dependent stiffness gradients between high- and low-confinement systems. (A) Schematics of the 20 nm and 600 nm films used in FEA, representing high- and low-confinement systems respectively (the thick film case is mimicked in MD using soft bottom confinements). FEA local stiffness profiles for (B) high and (C) low confinement systems. MD local stiffness profiles for (D) high and (E) low confinement systems. The FEA sweeps in (C) also include elastic models to demonstrate the effect of dissipation.

To confirm that the similarities between FEA and MD hold for ξ_{int} measurements, we performed additional MD simulations. As the option of modeling a 600 nm film is not directly available in MD due to the computational limit, we instead vary the strength of the confinement of the bottom wall of the MD model to mimic differing degrees of confinement accessible via FEA. We introduce a weaker bottom substrate that relaxes the hardness spring confinement (i.e. the spring constant is lowered from 1000 kcal/mol-Å^2 to 0.5 kcal/mol-Å^2 – see Section 2.1) and thus introduce a degree of compliance to the bottom layer of the polymer system. The low temperature ξ_{int} measurements are almost identical (58 nm and 56 nm) in the strong (Fig. 6D) and weak (Fig 6E) confinement cases. The weaker spring force mimics an increased film thickness via compliance to an extent but still limits the volume of activated polymer by an indentation. Thus, some confinement effects will remain, which may explain the differences in the trend compared to Fig. 6C. We also expect that there is a free surface effect that will lower G' in the MD simulations that is not accounted for in the FEA. As a result, the activated volume is likely lower and reduces the impact of increasing the compliance of the bottom substrate.

We note that a difference in magnitude of normalized stiffness is evident between FEA (Fig. 6B and 6C) and MD (Fig. 6D and 6E) simulations. In theory, it is possible that differences in the exact composition of the lateral substrate, and the differences in G' and G'' of the polymers between FEA and MD systems, may contribute to this different magnitude. However, the difference is particularly remarkable in the thin film FEA case (Fig. 6C), which exhibits very low normalized stiffness magnitudes near the interface and ξ_{int} values that extend less than 60nm. To understand this result, we note that the absolute stiffness k values obtained from indentation sweeps on the 20 nm films are substantially and systematically higher than on the 600 nm films (which is sufficiently thick that an increase in thickness does not change the measured stiffness) at the same

T (Fig. S5A and S5B); indeed the asymptotic "far field" value (away from the substrate) for stiffness is 6.2 and 7.8 times larger in the thin film compared to the thick film at 391.8 K and 406.8 K respectively. These findings indicate that having an extremely close rigid substrate under the indenter artificially raises the "effective stiffness" values obtained from indentation and as such weakens the impact of the lateral substrate on ξ_{int}. We note that the MD results show similar trends with respect to absolute stiffness (Fig. S5C and S5D) as the FEA analysis. The relative differences in *k* between the high and low confinement cases are less dramatic than the FEA case as the free-surface effect will reduce the impact of the confining bottom substrate in the MD but is not present in the FEA. This may also explain the reduced impact of the bottom substrate in the MD model compared to the FEA (Fig. 6E). It is noted that the both the MD and FEA simulations are conducted in 2D which will naturally promote geometric confinement compared to experimental systems, which occur in 3D. A stronger confinement effect in 2D systems is expected due to the tip acting as an infinitely long cylindrical indenter, whereas in experiments the tip is typically spherical, reducing the effective polymer volume confined by the tip and a neighboring substrate. It is also expected that changing the tip radius from what is used here ($R = 20\ nm$) will influence the impact of confinement on the measured stiffness. As has been previously observed in experimental systems,[13] a larger tip radius may exacerbate the structural contributions from a substrate to the measured stiffness in high confinement cases.

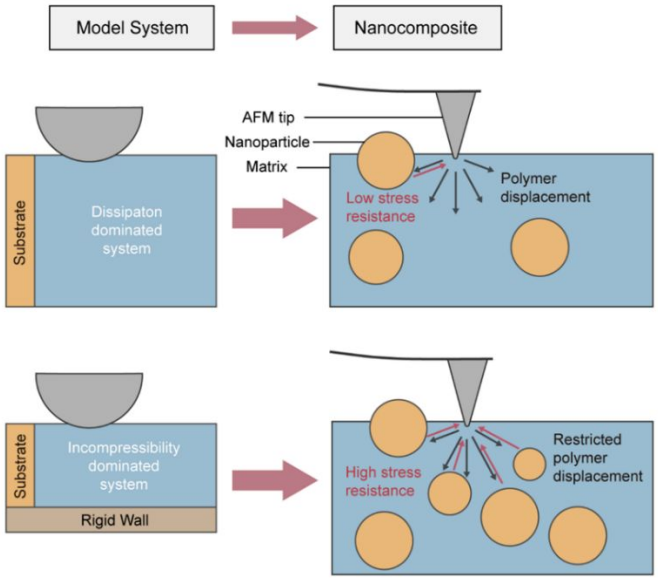

Figure 7. Possible implications of our findings on the nanoindentation analysis of stiffness gradients in polymer nanocomposites at high *T* or with incompressible matrix polymers. Indentation study of nanocomposite systems at low particle loadings will facilitate load dissipation via polymer displacement, whereas systems with high particle loadings will enhance stiffness readings due to build-up of hydrostatic pressure, resulting in an increase in the observed stiffness gradient.

These results have interesting possible consequences on the nanoindentation analysis of actual polymer nanocomposites, where particles are embedded in the matrix below the surface (Fig. 7) as well as supported thin films, where confinement will increase as film thickness decreases. The relationship between confinement, polymer incompressibility and viscoelastic state may help explain the wide range of ξ_{int} measured in previous studies (Table 1). In an analogous fashion, we hypothesize that mechanical tests on polymer composites and nanocomposites at high filler loadings are likely to result in hydrostatic pressure build-ups that may cause an apparent increase in the measured ξ_{int} as the polymer moves from a glassy to rubbery regime with increased temperature. In accordance with our results, this would be exacerbated in systems involving larger indentation depths[38], larger indenter sizes[10], or indentations that occur over particles. Our results may explain the experimental findings of Huang et al.,[11] who found a temperature-dependent effect on ξ_{int} by performing nanoindentation experiments on a nanocomposite film near a visible particle. Additionally, they also find that ξ_{int} plateaus slightly after the T_g, possibly due to reaching the plateau in ν and tan δ as shown in our work. Our results may also partly explain the discrepancy

between the interphase length-scales described by Huang et al., and Xia et al., (30 ~ 60 nm)[10, 11] and those described by Cheng et al. (~ 200 nm)[6]. Cheng et al.'s study utilizes a thick film, avoiding the confinement of the rigid supporting wall, therefore resulting in a lower measured modulus and a greater stiffness gradient length-scale as shown in Fig. 5C; while both the experiment in Huang et al and the simulation in Xia et al consider highly confined systems. In addition, recent work that uses FEA to remove structural effects from experimental AFM data on similar low confinement systems from Zhang et al.[22], clearly demonstrates a non-zero ξ_{int}, reflecting chemical and molecular confinement effects beyond the effective ξ_{int} demonstrated here.

4. Conclusion

In summary, we have shown that increasing the temperature of a confined polymer system in MD changes the viscoelastic state and induces incompressibility and viscous dissipation, which may create two distinct behaviors in ξ_{int} depending on the degree of confinement in the polymer. In highly confined systems, there is insufficient polymer volume to dissipate stress through intermolecular motion, thus causing hydrostatic pressure build-up and enhancement of the measured ξ_{int} with increasing temperature. In less confined systems, sufficient polymer volume allows more viscous dissipation of stress as molecules can move freely, thus reversing the trend of the measured ξ_{int} with temperature. The clear differences in the stiffness gradient polymers under different confinement scenarios suggest that the concept of thin film-nanocomposite equivalence as determined via T_g gradients may be more convoluted when applied to local nanomechanical measurements by indentation, and underline the need for caution when undertaking such analyses. Employing complementary simulations incorporating relevant

structural features will be helpful in interpretation of the underlying polymer physics from experimental data.

Conflicts of Interest

There are no conflicts of interest to declare.

Acknowledgements

The authors acknowledge support by the National Institute of Standards and Technology (NIST) through the Center for Hierarchical Materials Design (CHiMaD), as well as a computational grant from Quest HPC Systems at Northwestern University. D.W.C. would like to acknowledge a Ryan Fellowship from the International Institute for Nanotechnology at Northwestern University, a Fulbright Program grant sponsored by the Bureau of Educational and Cultural Affairs of the United States Department of State, and support from Goodyear Rubber and Tire Company (PO#4510883960 // Agreement 12 - 3/31/15). W.X. would like to acknowledge support from the NIST-CHiMaD Postdoctoral Fellowship. R. K. and J.S. would like to acknowledge Dr. Min Zhang and Dr. Pavan Kolluru at Northwestern University for helpful correspondence throughout the work.

References

1. O. K. C. Tsui, *Polymer thin films*, World Scientific, 2008.
2. W. Xia and S. Keten, *Extreme Mechanics Letters*, 2015, **4**, 89-95.
3. D. Paul and L. M. Robeson, *Polymer*, 2008, **49**, 3187-3204.
4. S. Watcharotone, C. D. Wood, R. Friedrich, X. Q. Chen, R. Qiao, K. Putz and L. C. Brinson, *Advanced Engineering Materials*, 2011, **13**, 400-404.
5. C. D. Wood, L. Chen, C. Burkhart, K. W. Putz, J. M. Torkelson and L. C. Brinson, *Polymer*, 2015, **75**, 161-167.
6. X. Cheng, K. W. Putz, C. D. Wood and L. C. Brinson, *Macromolecular Rapid Communications*, 2015, **36**, 391-397.
7. M. Zhang, S. Askar, J. M. Torkelson and L. C. Brinson, *Macromolecules*, 2017.
8. S. Askar and J. M. Torkelson, *Polymer*, 2016, **99**, 417-426.
9. M. Qu, F. Deng, S. M. Kalkhoran, A. Gouldstone, A. Robisson and K. J. Van Vliet, *Soft Matter*, 2011, **7**, 1066-1077.
10. W. Xia, J. Song, D. D. Hsu and S. Keten, *Macromolecules*, 2016, **49**, 3810-3817.
11. H. Huang, I. Dobryden, N. Ihrner, M. Johansson, H. Ma, J. Pan and P. M. Claesson, *J. Colloid Interface Sci.*, 2017, **494**, 204-214.
12. P. F. Brune, G. S. Blackman, T. Diehl, J. S. Meth, D. Brill, Y. Tao and J. Thornton, *Macromolecules*, 2016, **49**, 4909-4922.
13. H. K. Nguyen, S. Fujinami and K. Nakajima, *Polymer*, 2016, **87**, 114-122.
14. M. Zhang, S. Askar, J. M. Torkelson and L. C. Brinson, *Macromolecules*, 2017, **50**, 5447-5458.
15. S. Cheng, V. Bocharova, A. Belianinov, S. Xiong, A. Kisliuk, S. Somnath, A. P. Holt, O. S. Ovchinnikova, S. Jesse and H. Martin, *Nano letters*, 2016, **16**, 3630-3637.
16. A. Bansal, H. Yang, C. Li, K. Cho, B. C. Benicewicz, S. K. Kumar and L. S. Schadler, *Nature Materials*, 2005, **4**, 693-698.
17. J. M. Torres, C. M. Stafford and B. D. Vogt, *Acs Nano*, 2009, **3**, 2677-2685.
18. D. D. Hsu, W. Xia, S. G. Arturo and S. Keten, *Journal of Chemical Theory and Computation*, 2014, **10**, 2514-2527.
19. M. Rubinstein and R. H. Colby, *Polymer physics*, Oxford University Press New York, 2003.
20. D. J. Evans and G. Morriss, *Physical Review A*, 1984, **30**, 1528.
21. P. F. Brune, G. S. Blackman, T. Diehl, J. S. Meth, D. Brill, Y. F. Tao and J. Thornton, *Macromolecules*, 2016, **49**, 4909-4922.
22. M. Zhang, Y. Li, P. V. Kolluru and L. C. Brinson, *Macromolecules*, 2018.
23. L. Li, L. M. Encarnacao and K. A. Brown, *Applied Physics Letters*, 2017, **110**, 043105.
24. H. Zhao, X. Li, Y. Zhang, L. S. Schadler, W. Chen and L. C. Brinson, *APL Materials*, 2016, **4**, 053204.
25. NanoMine, http://nanomine.northwestern.edu:8000/, (accessed July, 2018).
26. P. J. Daivis and B. Todd, *The Journal of chemical physics*, 2006, **124**, 194103.
27. J. Song, D. D. Hsu, K. R. Shull, F. R. Phelan, J. F. Douglas, W. J. Xia and S. Keten, *Macromolecules*, 2018, **51**, 3818-3827.
28. H. C. Tseng, J. S. Wu and R. Y. Chang, *Physical Chemistry Chemical Physics*, 2010, **12**, 4051-4065.
29. M. P. Allen and D. J. Tildesley, *Computer simulation of liquids*, Oxford university press, 2017.
30. M. Falk and J. Langer, *Physical Review E*, 1998, **57**, 7192.
31. G. J. Papakonstantopoulos, R. A. Riggleman, J.-L. Barrat and J. J. de Pablo, *Physical Review E*, 2008, **77**, 041502.
32. A. Stukowski, *Modelling and Simulation in Materials Science and Engineering*, 2009, **18**, 015012.
33. P. C. Chung and P. F. Green, *Macromolecules*, 2015, **48**, 3991-3996.

34. P. C. Chung, E. Glynos and P. F. Green, *Langmuir*, 2014, **30**, 15200-15205.
35. J. D. Ferry, *Viscoelastic properties of polymers*, John Wiley & Sons, 1980.
36. P. Mott, J. Dorgan and C. Roland, *Journal of Sound and Vibration*, 2008, **312**, 572-575.
37. C. A. Clifford and M. P. Seah, *Nanotechnology*, 2009, **20**, 145708.
38. C. A. Clifford and M. P. Seah, *Nanotechnology*, 2006, **17**, 5283-5292.

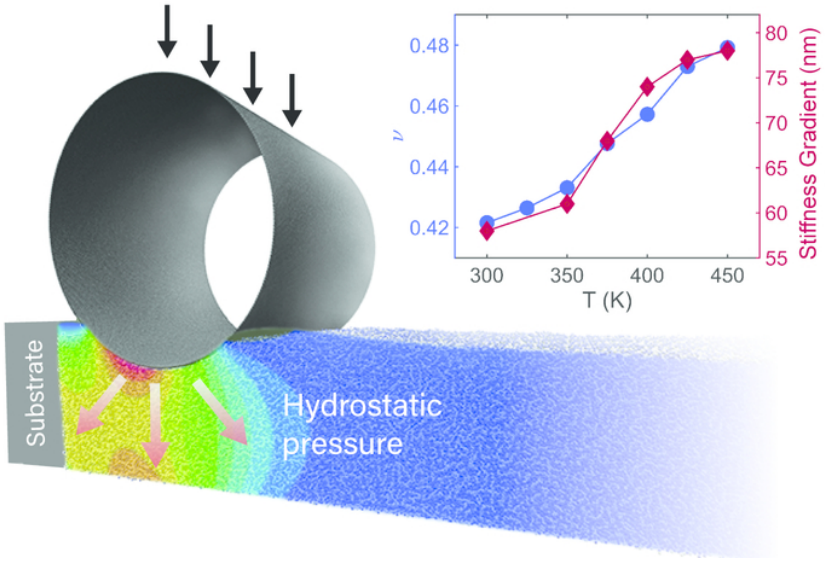

70x40mm (300 x 300 DPI)